

## NUMERICAL INVESTIGATION OF 3D DROP-BREAKUP MECHANISMS USING A SHARP INTERFACE LEVEL-SET METHOD

J. M. Winter<sup>+</sup>, J. W. J. Kaiser<sup>\*</sup>, S. Adami<sup>†</sup>, N. A. Adams<sup>‡</sup>

Technical University of Munich  
Department of Mechanical Engineering  
Chair of Aerodynamics and Fluid Mechanics  
Boltzmannstraße 15, 85748 Garching, Germany  
<sup>+</sup> Correspondent author: josef.winter@tum.de

### ABSTRACT

We present two- and three-dimensional numerical simulation results of a shock-induced droplet breakup. We study the breakup mechanism for two different Weber numbers. Reynolds and Ohnesorge numbers are kept constant. We apply a conservative interface-interaction model to compute the exchange of momentum and energy between the two immiscible fluids water and air. The fluids are separated by a sharp interface (level set). A block-structured multiresolution scheme is used to adapt the mesh to the evolving flow field.

We verify our simulation setup using a two-dimensional shock-induced breakup with a high Weber number, which is compared to experimental and numerical data. Simulation results show that the flattening of the droplet, which is the first stage of the droplet breakup, is independent of the Weber number. Once interfacial instabilities appear at the water-air interface, surface-tension effects play a dominant role in determining the second stage of the breakup. For small surface-tension forces, the droplet breakup occurs in the shear-induced entrainment (SIE) regime. Shear instabilities grow near the droplet equator, and form the sheet which is characteristic for this regime. For large surface-tension forces, the droplet breakup occurs in the Rayleigh-Taylor piercing (RTP) regime. Surface tension forces suppress the growth of the sheet, and lead instead to a smooth water-air interface. At later stages, the onset of the characteristic bag shape is observed.

### INTRODUCTION

Aerodynamic fragmentation, i.e. the breakup of an initially spherical drop into smaller droplets, is a matter of interest for a wide range of technological applications and environmental phenomena, for example in internal liquid fuel combustion engines or for the splatter of rain drops on supersonic aircrafts. The underlying fluid mechanical instability mechanism that dominates the breakup process depends on the ratio of aerodynamic forces, viscous forces, and surface tension. Five main breakup modes are classically distinguished: vibrational, bag, multimode, shear stripping, and catastrophic (Guildenbecher *et al.*, 2009). Dai & Faeth (2001) proposed that the multimode breakup is a transi-

tional mode from bag to sheet thinning, which occurs either as bag/plume breakup or plume/sheet-thinning. A reclassification of these breakup regimes was suggested by Theofanous (2011), motivated by the physical mechanisms which dominate the different breakup regimes: Rayleigh-Taylor piercing (RTP) and shear-induced entrainment (SIE). For lower ratios of aerodynamic forces to surface tension and viscous forces, RTP is the relevant instability mode for breakup (bag). With increasing aerodynamic forces, SIE becomes dominating (shear stripping). The multimode breakup occurs at the transition between these two mechanisms. The exact interplay between these two instability mechanisms remains, however, an open question.

Due to the inherent difficulties of analyzing droplet breakup experimentally - especially small spatial and temporal scales - and increasing computational capabilities, direct numerical simulation emerges as possible choice for detailed investigations. Many studies so far have been limited to two dimensions (2D) or assume axisymmetry (Aalburg *et al.*, 2003, e.g.). Khosla *et al.* (2006) were among the first to perform fully three-dimensional simulations. Their investigations focused on the low Weber-number range. Meng & Colonius (2018) performed a detailed fully three-dimensional simulation of drop breakup in the SIE regime, using a non-adaptive cylindrical grid to solve the compressible Euler equations and the volume-of-fluid (VOF) approach for interface capturing. First three-dimensional results in the RTP regime have recently been published by Yang *et al.* (2017), assuming incompressible fluid flow.

In this work, we investigate drop breakup dynamics in the RTP and SIE regimes. Based on our previous work (Kaiser *et al.*, 2017), two- and three-dimensional simulations of a water droplet in air flow are conducted for different Weber numbers. We approximate the compressible Navier-Stokes equations with a finite-volume approach. A fifth-order WENO scheme for flux reconstruction at cell faces ensures high-order representation of small flow scales, while overall computational efficiency is improved by our wavelet-based block-structured multiresolution scheme with adaptive local time-stepping. This allows for adapting our mesh to the changing flow field, including instantaneous time-step size adaptation. The phase interface is described by a level-set function, and explicit interface exchange terms are formulated to model the interface interaction. After validating the multi-phase model, we compare

---

\*jakob.kaiser@tum.de

†stefan.adami@tum.de

‡nikolaus.adams@tum.de

our results in the SIE regime to results of Meng & Colonius (2018) and Meng & Colonius (2015). Then, we analyze the breakup dynamics at lower Weber numbers in the RTP regime.

## METHODOLOGY

The problem is governed by the compressible Navier-Stokes equations including surface tension

$$\frac{\partial \mathbf{U}}{\partial t} + \nabla^T \cdot \mathbf{F}(\mathbf{U}) + \nabla^T \cdot \mathbf{F}_v(\mathbf{U}) = \mathbf{S}(\mathbf{U}) \quad (1)$$

with

$$\mathbf{U} = \begin{pmatrix} \rho \\ \rho \mathbf{u} \\ E \end{pmatrix} \quad \mathbf{F}(\mathbf{U}) = \begin{pmatrix} \mathbf{u}\rho \\ \rho \mathbf{u} \otimes \mathbf{u} + p\mathbf{I} \\ \mathbf{u}(E + p) \end{pmatrix}$$

$$\mathbf{F}_v(\mathbf{U}) = \begin{pmatrix} 0 \\ \mathbf{T} \\ \mathbf{T} \cdot \mathbf{u} \end{pmatrix} \quad \mathbf{S}(\mathbf{U}) = \begin{pmatrix} 0 \\ \kappa \sigma \mathbf{N} \\ \kappa \sigma \mathbf{N} \cdot \mathbf{u} \end{pmatrix}.$$

The set of equations is closed by applying the stiffened gas EOS

$$p = (\gamma - 1)\rho e - \gamma p_\infty. \quad (2)$$

$\rho$  is the density,  $\mathbf{u}$  the velocity vector,  $E$  the total energy,  $p$  the pressure,  $\mathbf{I}$  the identity matrix,  $\mathbf{T}$  the viscous stress tensor,  $\kappa$  the local interface curvature,  $\sigma$  the surface tension coefficient,  $\mathbf{N}$  the local normal vector on the interface,  $\gamma$  the ratio of specific heats,  $e$  the internal energy, and  $p_\infty$  the reference pressure for the stiffened gas EOS. Material parameters for the compressible Navier-Stokes equations and the stiffened EOS are given in Table 1. Parameters for air are chosen at the post-shock temperature. Parameters for water are chosen at 293.15 K, assuming that the breakup time scale is much smaller than the convective time scale for heat transport.

We apply a finite-volume discretization scheme on cubic cells with characteristic flux projection for the hyperbolic part (Roe, 1981) and global Lax-Friedrichs (GLF) flux splitting. Cell face fluxes are reconstructed with the fifth-order WENO scheme (Jiang & Shu, 1996). It applies low-dissipative, high order stencils in smooth flow regions, while falling back to non-linear convex combinations of lower-order stencils in regions with large spatial gradients. The dissipative terms are discretized with a fourth-order central-difference scheme. The third-order Runge-Kutta Total Variation Diminishing scheme is applied for time discretization (Gottlieb & Shu, 1998). The timestep size is limited by the CFL-condition

$$\Delta t = \text{CFL} \frac{1}{\sum_i \frac{|u_i + c|_\infty}{\Delta x_i}} \quad (3)$$

with the speed of sound  $c$  and the cell width in  $i$ -direction

$\Delta x_i$ . The CFL-number is set to  $\text{CFL} = 0.4$ .

A level-set function,  $\phi$ , is employed to capture the propagation of the drop interface.  $\phi$  designates the signed distance between the cell center and the interface, with  $\phi = 0$  being the interface and  $|\nabla \phi| = 1$ . An advection equation

$$\frac{\partial \phi}{\partial t} + \mathbf{u}_\phi \cdot \nabla \phi = 0 \quad (4)$$

describes the evolution of the level-set field, with  $\mathbf{u}_\phi$  being the evolution velocity of the level-set. This velocity is obtained from a two-material Riemann at the phase interface Hu & Khoo (2004). The level-set field is reinitialized after every timestep to maintain the signed distance property (Sussman *et al.*, 1994). The level-set gradient is computed with a fifth-order WENO scheme to maintain small structures during reinitialization. The interaction between the two fluids is solved based on the sharp-interface model of Hu *et al.* (2006) with the extension for viscous and capillary forces of Luo *et al.* (2015). They formulate explicit exchange terms for each entry of the state vector  $\mathbf{U}$ , thus maintaining a sharp interface. Cell face fluxes close to the interface are reconstructed by utilizing ghost cells across the interface (Fedkiw *et al.*, 1999).

We apply a block-structured wavelet-based multi-resolution method for achieving efficient high-resolution simulations (Rossinelli *et al.*, 2011). Based on the original approach of Harten (1994), cell-averaged data ( $\bar{U}$ ) on a coarser refinement level  $l$  can be computed from a finer refinement level  $l + 1$  using the projection operator

$$P_{l+1 \rightarrow l} : \bar{U}_{l+1} \rightarrow \bar{U}_l \quad (5)$$

and cell-averaged data on level  $l + 1$  can be estimated from level  $l$  using the prediction operator

$$P_{l \rightarrow l+1} : \bar{U}_l \rightarrow \hat{U}_{l+1}. \quad (6)$$

The difference between predicted and exact data motivates the definition of the so-called details

$$\bar{d}_{l,i} = \bar{U}_{l,i} - \hat{U}_{l,i}. \quad (7)$$

They are an estimate for the spatial accuracy of the current mesh on level  $l + 1$ . If they are larger than a pre-defined level-dependent threshold, the solution is too inaccurate and additional grid points are added. If they are smaller grid points are removed. For example, when droplets move further downstream, the mesh is refined locally, while regions further upstream are coarsened. This improves overall computational efficiency of our aerobreakup simulations, as the grid can adapt to flow field features, which appear during the breakup process, and the deforming drop.

## DIMENSIONLESS PARAMETERS AND DROPLET DESCRIPTION

The drop breakup process is determined by the interplay of aerodynamic forces, viscous forces, and surface tension. Three non-dimensional numbers are therefore used to

Table 1. Material parameter.

Fluid	$p_0$ [Pa]	$\rho_0$ [kg]	$\gamma$ [-]	$p_\infty$ [GPa]	$\mu$ [ $10^{-3}$ Pa s]	$\sigma$ [ $10^{-3}$ N/m]	
Water	101325	1000	6.12	0.343	4.1	SIE	72.75
					111	RTP	533.9
Air	101325	1.204	1.4	0.0	0.0103		

distinguish the different breakup modes, which are the Weber number

$$We = \frac{\rho_g u_g^2 d_0}{\sigma}, \quad (8)$$

the Reynolds number

$$Re = \frac{\rho_g u_g d_0}{\mu_g}, \quad (9)$$

and the Ohnesorge number

$$Oh = \frac{\mu_l}{\sqrt{\rho_l d_0 \sigma}}. \quad (10)$$

Indices  $l$  and  $g$  denote liquid and gas phase, respectively,  $d_0$  the initial drop diameter, and  $\mu$  the dynamic viscosity. To compare the breakup behavior of a droplet for different dimensionless numbers, length scales are non-dimensionalized by the initial drop diameter  $x^* = x/D_0$ , velocities by the post-shock velocity  $u^* = u/u_s$ , and time-scales by

$$t^* = \frac{t}{\frac{D_0}{u_s} \sqrt{\frac{\rho_l}{\rho_s}}}.$$

Here,  $\rho_l$  and  $\rho_s$  denote the densities of the droplet and the post-shock air, respectively.

For validation, we compare the upstream-stagnation-point  $\Delta x_{sp}^*$  and the center-of-mass drift  $\Delta x_c^*$  to experimental and numerical data (Igra & Takayama, 2001; Meng & Colonius, 2015). The center of mass is computed following

$$x_c = \frac{\int_{\Omega_l} \rho x dV}{\int_{\Omega_l} \rho dV}$$

considering only the liquid subdomain.

## TWO-DIMENSIONAL SIMULATIONS IN THE SIE AND RTP REGIMES

Igra & Takayama (2001) investigated the breakup of a  $d_0 = 4.8$  mm water column in the wake of a  $Ma = 1.47$  shock wave in air, which causes breakup in the SIE regime. This setup has been widely investigated numerically, though often excluding viscous forces and surface tension due to small  $Oh$  and large  $Re$  numbers (Meng & Colonius, 2018, e.g.). As both effects are relevant for RTP, we consider them

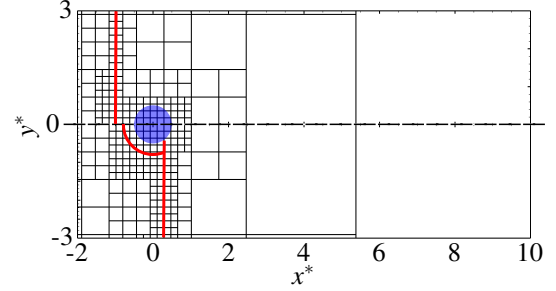


Figure 1. Sketch of the simulation domain, including the multiresolution mesh and most important flow field features. Upper half: initialization. Lower half: adapted grid shortly after the impinging of the shock on the drop. The droplet is sketched in blue, the shock in red (Kaiser *et al.*, 2017).

in our SIE simulations. A sketch of the two-dimensional simulation domain is given in Fig. 1, assuming line symmetry and including a possible mesh resolution. The drop is sketched in blue, the progressing shock wave in red. The mesh adapts to the progressing shock wave, refining the grid around the shock, and coarsening it in the post-shock region where the flow field yields small local gradients. For the breakup in the SIE regime, we choose dimensionless parameters of  $We = 7339$ ,  $Oh = 6.9 \times 10^{-3}$ , and  $Re = 229485$ . For the breakup in the RTP regime, we increase surface-tension effects to obtain  $We = 12$  and increase viscous effects inside the droplet to keep  $Oh$  constant.  $Re$  is the same as in the SIE regime. For both setups, the shock Mach number is  $Ma = 1.47$  as in the experiment. The mesh resolution is  $D_0/\Delta x = 100$ , with an overall resolution of  $2048 \times 1024$  for the entire domain. The resulting parameters for the surface tension coefficient and the viscosity of the droplet are given in table 1.

Fig. 2 shows leading-edge (top) and center-of-mass drifts (bottom) for the SIE regime in comparison to literature results (left half). The right half compares the drifts for the two different breakup regimes. For the SIE regime, the leading edge drift  $\Delta x_{sp}^*$  agrees well with literature results. The center-of-mass drift  $\Delta x_c^*$  is delayed compared to literature results, but shows overall similar behavior. The decreasing Weber number has a minor impact on  $\Delta x_{sp}^*$  for  $t^* < 0.7$ . At later instants, the breakup in the RTP regime yields a larger leading-edge drift than in the SIE regime. A similar behavior is observed for the center-of-mass drift. For  $t^* < 0.7$ , both curves overlap. Afterwards, the SIE regime yields a larger  $\Delta x_c^*$ . This indicates that the very early stages are dominated by viscous and inertial effects. Hence, the drift behavior for both regimes overlaps. At later stages, surface tension effects have a significant influence on the drop-deformation process in the RTP regime, causing the observed deviation to the SIE regime.

Figures 3 and 4 show various instants of the breakup

process for the SIE and the RTP regime. The inner of the droplet is shown white. Its interface is highlighted black. The upper half of each image depicts the numerical schlieren in the vicinity of the droplet. The lower half shows the streamwise velocity field  $u^*$ . At  $t^* = 0.25$  a flattening of the droplet is visible for both breakup modes. This originates from a non-uniform pressure distribution along the drop circumference (Meng & Colonius, 2015). At this instant, a cusp in the drop interface at the equatorial plane is already visible in the SIE regime. It is a first indicator for a sheet stripping mechanism (Chen, 2008) and grows up to  $t^* = 0.75$ . During that time additional cusps at the upstream and downstream hemisphere of the droplet develop. Cusps at the upstream hemisphere are moving towards the equatorial plane till they merge with the emerging tip at the equator and form a single sheet ( $t^* = 1.0$ ) characteristic for the SIE regime. The tip of the sheet moves downstream before it breaks up or disappears since being underresolved ( $t^* > 1.0$ ). For the RTP regime, higher viscous and surface tension forces at the interface suppress the development of cusps. Instead, starting from  $t^* = 1.0$  the upstream side of the droplet adopts a concave shape. For later times, the concavity gets enforced and onset of bag growth can be observed.

The deformation of the droplet leads to unsteady vortex shedding in the wake of the droplet and creates a recirculation zone (Meng & Colonius, 2018). This is visible for both the RTP and the SIE regime. The recirculation zone is initially supersonic. Later, the deflection of the flow close to the droplet forms a shock with a subsonic region. For the SIE case, in addition to this wake recirculation zone multiple smaller recirculation zones can be observed at the droplet interface which emerge at the growing cusps. At the tip of the sheet created by the merging cusps, a recirculation zone develops, too ( $t^* = 1.0$ ). This recirculation zone disappears at later times. Also, the main recirculation zone and the shock therein stabilize. While in the beginning the vortex shedding for SIE and RTP is similar, the RTP case does not show additional recirculation zones besides the main recirculation zone due to the missing cusps at the droplet interface. The stabilization of the main recirculation and the shock therein sets in earlier for the RTP case.

### THREE-DIMENSIONAL SIMULATIONS IN THE SIE AND RTP REGIME

Three-dimensional simulations in the SIE and RTP regime are performed to evaluate the performance of our models in three dimensions. Initial and boundary conditions are the same as for the two-dimensional simulations. The droplet resolution is  $D_0/\Delta x = 50$ , the overall domain resolution is  $1024 \times 1024 \times 1024$ .

Fig. 5 shows the deformed droplet for the SIE (upper half,  $t^* = 1$ ) and RTP (lower half,  $t^* = 2$ ) breakup regimes. The left half shows the isosurface of the droplet (blue) and the zero-isosurface of the axial velocity, colored by the radial velocity, in an isometric view, and the right half the droplet in a side view. Numerical results yield distinct differences in the droplet deformation for the breakup regimes, which were already observed in the two-dimensional setup. For the SIE regime, the droplet develops a mushroom-like shape, with a distinct, compact recirculation zone in its wake. This upstream jet impinges onto the droplet at the downstream stagnation point, leading to a concave interface shape there. At the edge of the droplet equator, the onset of

the sheet stripping breakup is visible. The sheet is advected downstream, where it breaks up or is removed by the numerical scheme as it is underresolved. This agrees well with the results of the two-dimensional simulations and the results of Meng & Colonius (2018).

The drop breakup in the RTP regime occurs at larger timescales, which is why the interface is shown here at  $t^* = 2$  (Guildenbecher *et al.*, 2009). The droplet is nearly planar on the upstream side, with a small concave deformation near the center. This is potentially the onset of the bag growth which is expected for this Weber number. On the downstream side, the drop has a convex shape, and no sheet is stripped of at the droplet equator. A recirculation zone forms, too, which is stretched in axial direction. Strong unsteady vortex shedding causes the recirculation zone to locally detach from the downstream side of the deformed drop.

### CONCLUSIONS

We have presented numerical results of shock-induced droplet breakup for two different Weber numbers, at constant Ohnesorge and Reynolds numbers. The high Weber-number case corresponds to a breakup in the SIE regime, the low Weber-number case to a breakup in the RTP regime. We validated our results with experimental and numerical data. Then, we compared results of two- and three-dimensional simulations in the two regimes.

In our simulations, the flattening of the droplet, which is the first stage of the droplet breakup (Chen, 2008), is independent of the Weber number. Once interfacial instabilities appear at the water-air interface, surface-tension effects play a dominant role in determining the second stage of the breakup. For small surface-tension forces, the droplet breakup occurs in the SIE regime. Shear instabilities grow near the droplet equator, and form the sheet which is characteristic for this regime. For large surface-tension forces, the droplet breakup occurs in the RTP regime. Surface tension forces suppress the growth of the sheet, and lead instead to a smooth water-air interface. At later stages, the characteristic bag shape develops.

Our work shows the strong influence of surface tension forces on the growth of interfacial instabilities during the very early stages of the breakup, which then determine the later stages. In future work, we plan to further investigate the interplay of growing interfacial instabilities and surface tension forces during the early stages, and the later stages of the breakup. In addition, the effect of increasing Ohnesorge numbers will be analyzed, as dampening effects of a higher viscosity of the droplet fluid potentially limit the growth of interfacial instabilities.

### ACKNOWLEDGEMENTS

This project has received funding from the German Research Foundation (Deutsche Forschungsgesellschaft) and the European Research Council (ERC) under the European Union's Horizon 2020 research and innovation programme (grant agreement No. 667483). The authors gratefully acknowledge the Gauss Centre for Supercomputing e.V. for funding this project by providing computing time on the GCS Supercomputer SuperMUC at Leibniz Supercomputing Centre.

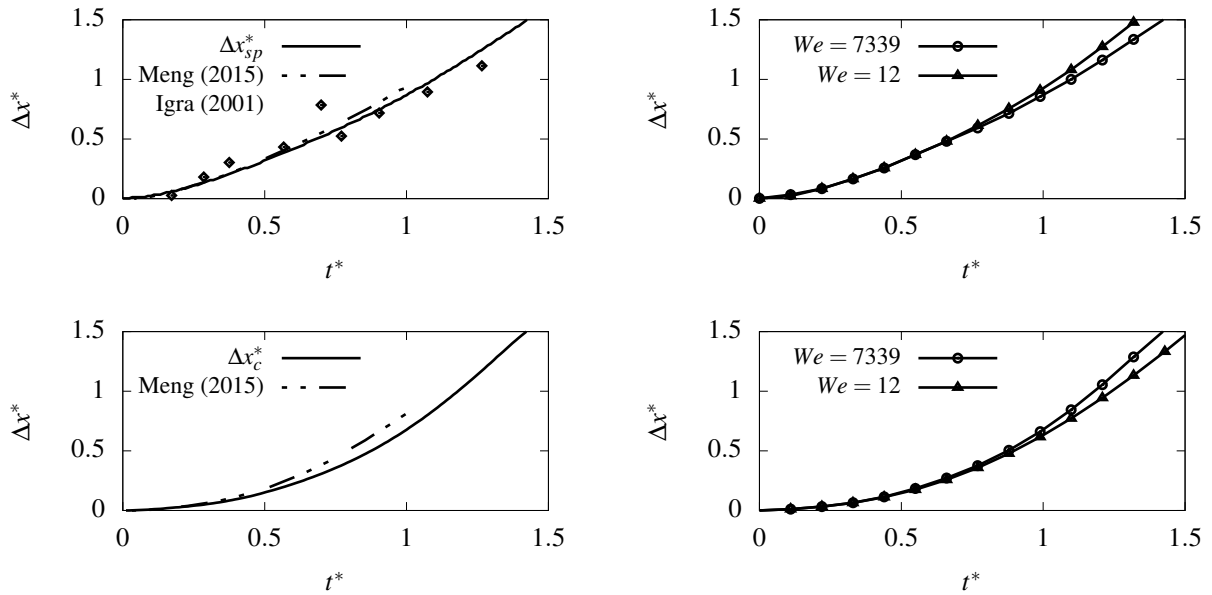


Figure 2. Leading edge drift for 2D SIE: own results and comparison to results of Igra & Takayama (2001) and Meng & Colonius (2015).

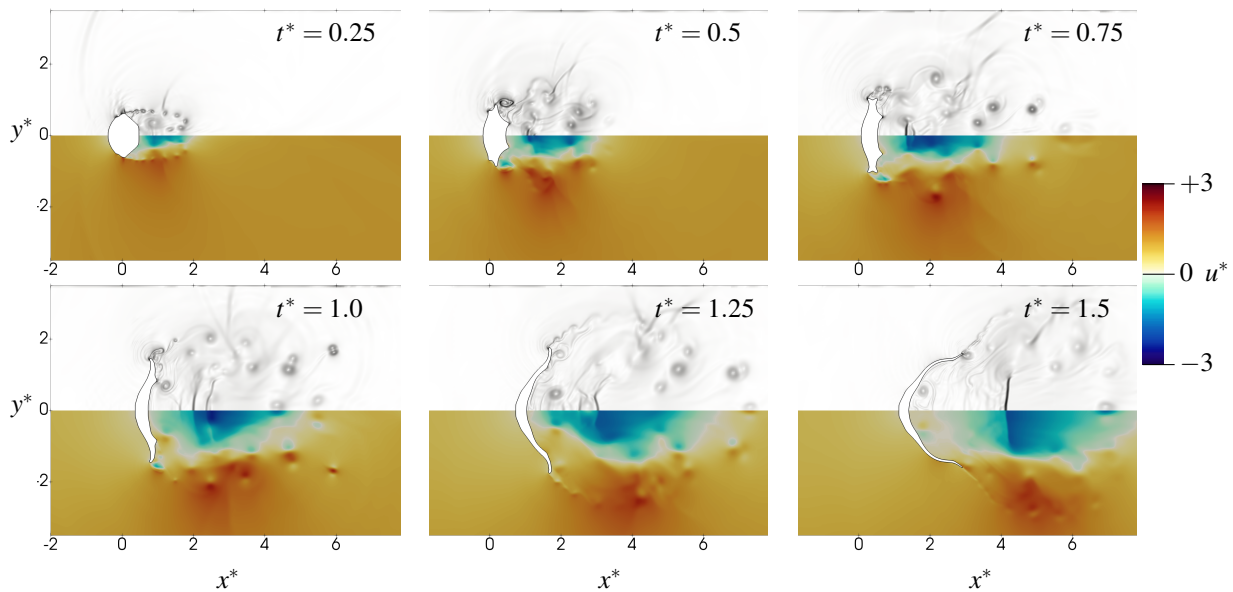


Figure 3. Time series for the SIE breakup mode with  $We = 7339$ .

## REFERENCES

- Aalburg, C., van Leer, B. & Faeth, G. M. 2003 Deformation and drag properties of round drops subjected to shock-wave disturbances. *AIAA J.* **41** (12), 2371–2378.
- Chen, H. 2008 Two-dimensional simulation of stripping breakup of a water droplet. *AIAA J.* **46** (5), 1135–1143.
- Dai, Z. & Faeth, G. M. 2001 Temporal properties of secondary drop breakup in the multimode breakup regime. *Int. J. Multiphase Flow* **27**, 217–236.
- Fedkiw, R. P., Aslam, T. D., Merriman, B. & Osher, S. 1999 A Non-oscillatory Eulerian Approach to Interfaces in Multimaterial Flows (The Ghost Fluid Method). *J. Comput. Phys.* **152** (2), 457–492.
- Gottlieb, Sigal & Shu, Chi-Wang 1998 Total variation diminishing Runge-Kutta schemes. *Mathematics of computation of the American Mathematical Society* **67** (221), 73–85.
- Guiltenbecher, D. R., López-Rivera, C. & Sojka, P. E. 2009 Secondary atomization. *Experiments in Fluids* **46** (3), 371–402.
- Harten, Ami 1994 Adaptive Multiresolution Schemes for Shock Computations. *Journal of Computational Physics* **115**, 319–338.
- Hu, X.Y. & Khoo, B.C. 2004 An interface interaction method for compressible multifluids. *Journal of Computational Physics* **198** (1), 35–64.
- Hu, X.Y., Khoo, B.C., Adams, N.A. & Huang, F.L. 2006 A conservative interface method for compressible flows. *J. Comput. Phys.* **219** (2), 553–578.
- Igra, D. & Takayama, K. 2001 Numerical simulation of shock wave interaction with a water column. *Shock Waves* **11** (3), 219–228.

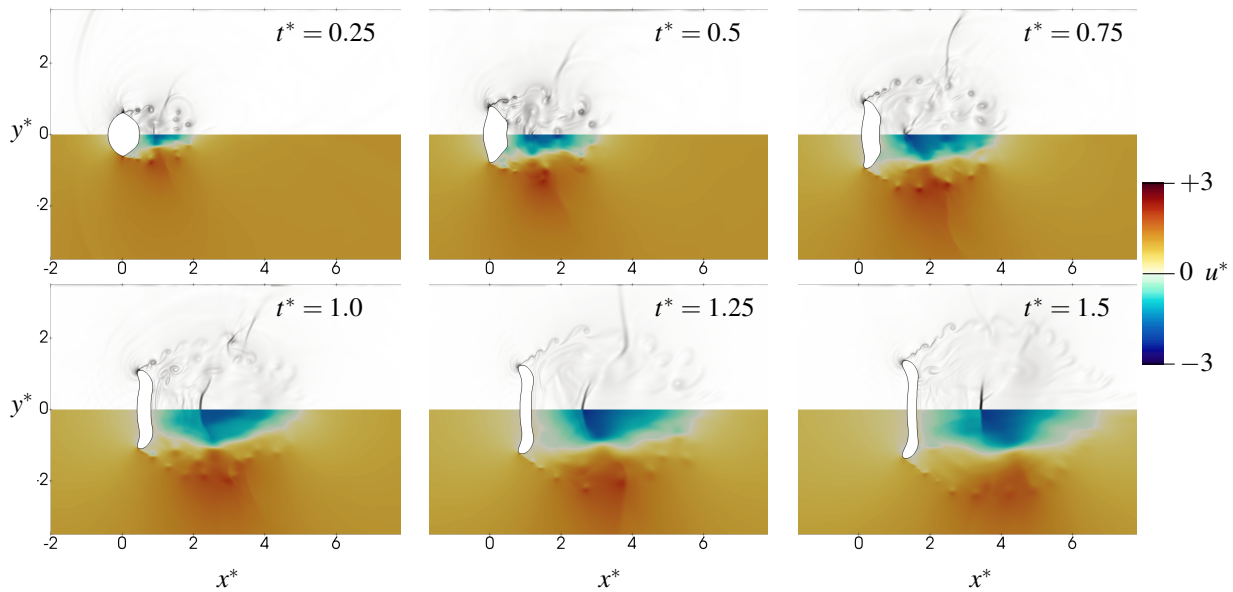


Figure 4. Time series for the RTP breakup mode with  $We = 12$ .

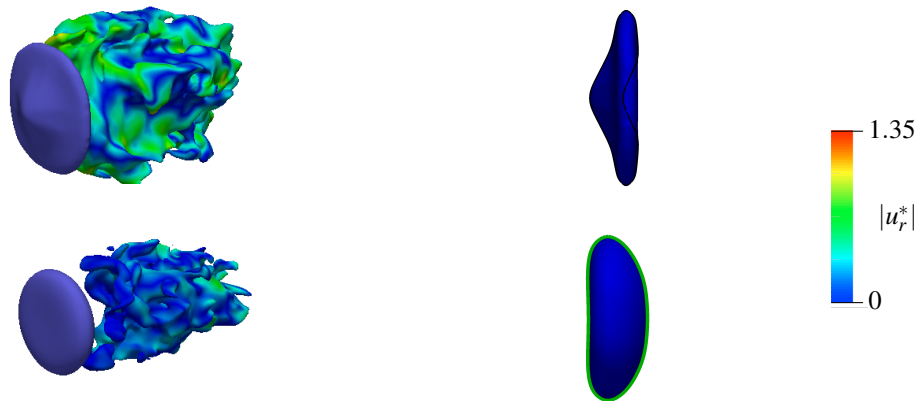


Figure 5. Droplet breakup in the SIE (upper half,  $t^* = 1$ ) and RTP (lower half,  $t^* = 2$ ) regime. Left: isosurface of the droplet (blue), and isosurface of the zero-axial velocity, coloured by the radial velocity. Right: isosurface of the droplet.

Jiang, G.-S. & Shu 1996 Efficient implementation of weighted ENO schemes. *Journal of Computational Physics* **126**, 202–228.

Kaiser, J.W.J., Adami, S. & Adams, N.A. 2017 Direct numerical simulation of shock-induced drop breakup with a sharp-interface-method. In *10th International Symposium on Turbulence and Shear Flow Phenomena, TSFP 2017*, pp. 1–6.

Khosla, Sachin, Smith, Clifford E. & Throckmorton, Ryan P. 2006 Detailed understanding of drop atomization by gas crossflow using the volume of fluid method. In *19th Annual Conference on Liquid Atomization and Spray Systems (ILASS-Americas), Toronto, Canada*.

Luo, J., Hu, X.Y. & Adams, N.A. 2015 A conservative sharp interface method for incompressible multiphase flows. *Journal of Computational Physics* **284**, 547–565.

Meng, J. C. & Colonius, T. 2015 Numerical simulations of the early stages of high-speed droplet breakup. *Shock Waves* **25**, 339–414.

Meng, Jomela C & Colonius, Tim 2018 Numerical simulation of the aerobreakup of a water droplet. *J. Fluid Mech*

**835**, 1108–1135.

Roe, Philip L. 1981 Approximate Riemann solvers, parameter vectors, and difference schemes. *Journal of computational physics* **43** (2), 357–372.

Rossinelli, D., Hejazialhosseini, B., Spampinato, D. G. & Koumoutsakos, P. 2011 Multicore/multi-gpu accelerated simulations of multiphase compressible flows using wavelet adapted grids. *J. Sci. Comput.* **33** (2), 512–540.

Sussman, Mark, Smereka, Peter & Osher, Stanley 1994 A Level Set Approach for Computing Solutions to Incompressible Two-Phase Flow. *J. Comput. Phys.* **114**, 146–159.

Theofanous, T.G. 2011 Aerobreakup of Newtonian and Viscoelastic Liquids. *Annual Review of Fluid Mechanics* **43** (1), 661–690.

Yang, Wei, Jia, Ming, Che, Zhizhao, Sun, Kai & Wang, Tianyou 2017 Transitions of deformation to bag breakup and bag to bag-stamen breakup for droplets subjected to a continuous gas flow. *International Journal of Heat and Mass Transfer* **111**, 884–894.